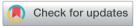
Journal of Materials Chemistry A



PAPER

View Article Online
View Journal | View Issue



Cite this: J. Mater. Chem. A, 2024, 12, 13139

A general strategy to prepare macro-/mesoporous materials from thermoplastic elastomer blends†

Anthony Griffin, ^{Da} Mark Robertson, Parker Frame, Guorong Ma, ^{Da} Kevin A. Green, Zhiqian Han, Sarah E. Morgan, Da Xiaodan Gu, Da Meng Wang and Zhe Qiang D*a

Hierarchically macro-/mesoporous (HMM) materials generally contain at least two distinct populations of pore sizes with ranges of 2-50 nm and >50 nm; they exhibit promising performance for various applications, such as water remediation and energy storage, due to the combined advantages of high surface area, pore accessibility, and porosity. Conventional synthesis of HMM materials typically utilize multiple templating agents to develop varied sizes of pores, often involving complex processes and the use of relatively expensive precursors with low recourse-efficiency, leading to significant challenges toward scaled production. Therefore, development of a simple approach for HMM materials synthesis is important for facilitating their commercialization and broad use. In this work, we demonstrate a generalizable method for the fabrication of HMM polymers and carbons using immiscible thermoplastic elastomer (TPE) blends, through incorporating a small amount of polystyrene-blockpolyisoprene-block-polystyrene (SIS) within the matrix of polystyrene-block-poly(ethylene-ranbutylene)-block-polystyrene (SEBS), followed by sulfonation-induced crosslinking. During this reaction, the presence of SIS not only leads to the formation of macropores from released gaseous products, but it also facilitates the selective degradation of polystyrene domains to develop ordered mesopores. These porous polymers can then be converted to HMM carbons upon pyrolysis, where ordered nanostructures can be retained. This approach to produce HMM materials can be generalized to different selections of TPE blends with varied precursor identity and molecular weight. Furthermore, we demonstrate that HMM polymers can be employed as sorbents for the efficient removal of heavy metals from aqueous systems, while their derived carbons are efficient for organic pollutant remediation. We believe this work demonstrates a simple and robust approach with great potential for the scaled manufacturing of HMM materials to enable their broad use in practical applications.

Received 8th March 2024 Accepted 1st May 2024

DOI: 10.1039/d4ta01590h

rsc.li/materials-a



Zhe Qiang

Dr Zhe Qiang is the SSCT Endowed Assistant Professor of Polymer Science and Engineering at the University of Southern Mississippi (USM). He received his M.S. and PhD degrees in Polymer Engineering from the University of Akron, and was a postdoc fellow at Northwestern University. His current research interests include developing sustainable solutions for addressing plastic waste and its associated environmental impacts. Since the start of his independent career, Dr Qiang has received many awards, including NSF EPSCOR Research Fellow, ACS PRF Doctoral New Investigator, Forbes 30 under 30 in Science, NSF CAREER award, AIChE 30 under 30, and SAMPE Young Professional of the Year.

[&]quot;School of Polymer Science and Engineering, The University of Southern Mississippi, Hattiesburg, MS, 39406, USA. E-mail: zhe.qiang@usm.edu

^bDepartment of Civil and Environmental Engineering, University of Pittsburgh, PA, 15261, USA

[†] Electronic supplementary information (ESI) available. See DOI: https://doi.org/10.1039/d4ta01590h

1. Introduction

Hierarchically macro-/mesoporous (HMM) materials have attracted broad interests in various applications, including catalysis,1-4 water remediation,5-8 energy storage,9-11 and biomedicine, 12-15 due to their collective advantages of tunable framework chemistry, uniform pore sizes and structures, enhanced pore accessibility, and relatively high surface areas,16 which can enable facilitated guest molecule sorption, transport, and diffusion within pore channels. In general, HMM materials can outperform their mesoporous counterparts due to the introduction of macropores,17 which lead to improved active site exposure that promotes enhanced transport along channels.18 For example, HMM carbons prepared through coassembly of bottlebrush block copolymers, linear block copolymers, and a phenol-formaldehyde resin to form "planet-satellite" morphologies were found to exhibit enhanced supercapacitor performance compared to monomodal porous carbons.19

A common approach to synthesize HMM materials is through the combined use of two or more templating agents for developing pores with distinct characteristic sizes.20 In most strategies, framework precursors are self-assembled with block copolymers (BCPs) and/or amphiphilic surfactants, which upon removal, can form mesopores and/or macropores.21 Moreover, a high internal phase emulsion (HIPE) templating method can be employed, ^{22,23} where monomers are polymerized in situ in the external phase of the emulsion followed by removal of the internal phase; in these systems synthesis of HMM materials can be achieved through coupling mesopore-forming compounds within an interconnected macroporous structure. While these conventional methods allow for the structural control in HMM materials through varying template/precursor selection and composition, they often require complex processes for material preparation, having low resource efficiency due to the removal of templating agents, as well as using expensive precursors.

Alternatively, direct conversion of self-assembled BCPs to mesoporous materials has attracted significant interest,24,25 due to its simplified reaction pathway compared to templatingbased methods. In these systems, BCPs typically contain at least two distinct segments for developing pores and frameworks respectively.26 Significant efforts in the direct synthesis of mesoporous materials have utilized polyacrylonitrile (PAN)based BCP precursors, specifically for ordered mesoporous carbon (OMC).27 The PAN majority phase can be readily crosslinked at elevated temperatures and acts as the carbon precursor while the minority phase directs nanostructure and forms pores upon pyrolysis. We note there are several strategies for preparing hierarchically porous polymers, 28-30 such as the combination of polymerization-induced microphase separation in addition to hyper-crosslinking with poly(4-vinylbenzyl chloride-co-divinylbenzene) and polylactide acid, which was shown to develop well-defined mesopores and micropores.³¹ Despite various synthetic routes and application demonstrations of hierarchically porous materials, the lack of a simple and costeffective method to produce HMM materials through direct pyrolysis at scale limits their transformative impacts. Addressing this challenge is essential to enable the scaled production of HMM materials and unlock their great potential for addressing various practical applications.³²⁻³⁵

In this work, we demonstrate a simple and universal strategy to prepare HMM materials using low-cost, commodity TPE blends as precursors, including porous polymers and carbons. Specifically, incorporation of a small amount of poly(styrene)block-poly(isoprene)-block-poly(styrene) (SIS) into a poly(styrene)-block-poly(ethylene-ran-butylene)-block-poly(styrene) (SEBS) matrix leads to macrophase separation between distinct BCPs, while retaining ordered nanostructures from selfassembly. Noteworthily, it is found that introducing SIS additives can result in selective cleavage of polystyrene domains upon sulfonation-induced crosslinking, leading to a streamlined approach to prepare HMM polymers. Through a subsequent pyrolysis step, HMM carbons can be produced containing ordered mesostructures; we note that SIS and SEBS are responsible for the formation macropores and mesopores, respectively. The impact of SIS loading content on the structure development of HMM materials is investigated, while the generalizability of this synthesis approach is confirmed by extending to other commodity TPE blend systems. Furthermore, HMM polymers can exhibit rapid sorption performance for the removal of heavy metals from water due to their large amount of negatively charged groups (sulfonic acid groups) on the pore surface, whereas HMM carbons can be employed for the removal of organic pollutants from aqueous systems, leveraging their high surface area and excellent pore accessibility.

2. Experimental section

2.1. Materials

Poly(styrene)-block-poly(ethylene-ran-butylene)-block-poly(styrene) (SEBS; $M_{\rm w}$: 118 000 g mol $^{-1}$, D: 1.59, $\phi_{\rm PS}=20$ wt%; $M_{\rm w}$: 89 000 g mol $^{-1}$, D: 1.56, $\phi_{\rm PS}=20$ wt%; $M_{\rm w}$: 100 000 g mol $^{-1}$, D: 1.67, $\phi_{\rm PS}=18$ wt%), poly(styrene)-block-poly(isoprene)-block-poly(styrene) (SIS; $M_{\rm w}$: 102 500 g mol $^{-1}$, D: 1.12, $\phi_{\rm PS}=14$ wt%), poly(methyl methacrylate) ($M_{\rm w}$: 38 000 g mol $^{-1}$), sulfuric acid (98%), rhodamine B (97%), nickel(ll) nitrate hexahydrate (99.9%), and toluene (>99.5%) were obtained from Sigma Aldrich. Cobalt(II) chloride hexahydrate (98–100%) and nickel(II) chloride hexahydrate (99.95%) were purchased from Thermo Scientific (Thermo Scientific, Waltham, MA). Nitric acid trace metal grade was obtained from Fisher Scientific (Fisher, Waltham, MA). Deionized (DI) water was obtained through a Millipore Sigma Milli-Q IQ 7003 ultrapure lab water purification system.

2.2. Synthesis of TPE blend-derived HMM materials

To synthesize HMM polymers using thermoplastic elastomer (TPE) blends, parent solutions of SEBS and SIS were first prepared at 5 wt% in toluene. Following this step, 10 g of the SEBS solution and a varied amount of SIS (between 0.1 and 1 g)

were blended, drop-cast onto Petri dishes, and dried overnight through slow solvent evaporation. These films were then removed for subsequent processing. For performing sulfonation-induced crosslinking reaction, 2 g of polymer blend film and 5 g of sulfuric acid were introduced, and the mixture was heated to 145 °C for varying amounts of time. Different amounts of sulfuric acid relative to polymer precursor ratios (ranging from 2.5 to 10 g) were also investigated to determine their influence of the crosslinking reaction, where a minimal influence was observed up until a minimum amount that is required for ensuring complete submersion of the polymer in the reaction mixture (Fig. S1†). Following sulfonation, crosslinked films were then washed with DI water three times in order to remove residual sulfuric acid and byproducts, which were then completely dried at 125 °C overnight. To prepare HMM carbons, crosslinked polymer was then carbonized using an MTI Corporation OTF-1200 \times tube furnace with a rate of 1 $^{\circ}$ C min⁻¹ to 600 °C and 5 °C min⁻¹ to 800 °C under a nitrogen environment, with a total carbonization time of 640 min. After reaching 800 °C, the furnace was naturally cooled down to room temperature.

2.3. General characterization

The chemical composition of prepared samples was investigated using a Thermo Nicolet 6700 Fourier transform infrared (FTIR) spectrometer with a Smart iTR attenuated total reflection accessory and a scan range of 4000-600 cm⁻¹. The measurements were performed through averaging over 32 scans at a resolution of 4 cm⁻¹. Atomic force microscopy (AFM) analysis of TPE blends was conducted using a Dimension Icon atomic force microscope (Bruker) in Peak-Force Tapping mode. Nano-Scope software was utilized for AFM scanning, and the images were analyzed and processed using NanoScope Analysis 3.0. Peak-Force Tapping mode imaging was performed using a sharp antimony (n) doped Si cantilever (RTESPA-300, nominal tip radius of 8 nm; nominal resonance frequency of 300 kHz; nominal spring constant 40 N m⁻¹) in a standard probe holder under ambient conditions with 256×256 data point resolution. To further study the nanostructure of TPE blends and their derived porous materials, small-angle X-ray scattering (SAXS) was carried out with a Xeuss 2.0 laboratory beamline (Xenocs Inc.) with an X-ray energy of 8.05 keV and a sample-to-detector distance of 3.86 m. The domain spacing of samples, d, was determined by $d = 2\pi/q^*$, where q^* is the scattering vector from the primary ordering peak's position within the scattering spectra. Scanning electron microscopy (SEM) was performed using a Zeiss Ultra 60 field-emission SEM to characterize the morphology of TPE blend derived porous samples with an accelerating voltage of 15 kV.

A Micromeritics Tristar II 3020 was used for performing nitrogen physisorption measurements at 77 K and carbon dioxide physisorption measurements at 273 K, where surface areas were determined by Brunauer-Emmett-Teller (BET) theory and non-local density functional theory (NLDFT) analysis with a carbon slit model was utilized for pore size distribution analysis. X-ray photoelectron spectroscopy (XPS)

characterization was performed by a ESCALAB Xi+ spectrometer (Thermo Fisher), equipped with a MAGCIS Ar+/Arn+ gas cluster ion sputter gun and a monochromatic Al X-ray source (1486.6 eV). A takeoff angle of 90° from the surface and a base pressure of 3 \times 10⁻⁷ mbar in the analysis chamber was set for spectral acquisition. Thermo Fisher Avantage software was used for spectral analysis.

2.4. Dye and ion sorption study

To evaluate the adsorption performance of HMM carbons, rhodamine B aqueous solutions with varied concentrations (from 50 to 800 mg L⁻¹) were prepared by dissolving the appropriate level of dye in 250 mL DI water. 0.02 g of porous carbon were introduced to 20 mL of dye solutions. To determine adsorption kinetics, aliquots at several time points were taken for the 50 mg L^{-1} concentration and then characterized with a Thermo Scientific Genesys 30 visible spectrometer to determine the maximum absorbance. Adsorption capacities were evaluated at several dye concentrations by shaking samples for 7 days, followed by determining quantity of dye adsorbed.

To evaluate the metal ion adsorption performance of HMM polymer, the metal chloride salts were dissolved in DI water and then diluted to prepare solutions with varying metal ion concentrations ranging from 5 mg L^{-1} to 5000 mg L^{-1} . For the adsorption kinetic experiment, 0.04 g of HMM polymer was added into 20 mL solutions containing 12 mg L^{-1} of metal ions in 250 mL Erlenmeyer flasks. These flasks were placed in a shaking incubator at 20 °C, agitating at a speed of 300 rpm (round per minute). At designated sampling time points, 100 μL solutions were taken from the flasks. After centrifugation for 20 s, 60 μL of the supernatant was collected and mixed with DI water and 1% nitric acid to achieve a final volume of 1800 µL. Residual metal ion concentrations were determined using Agilent 5100 ICP-OES (Agilent, Santa Clara, CA). For the adsorption isotherm experiment, 1 mL solutions with varying metal ion concentrations (5 mg L^{-1} to 5000 mg L^{-1}) were combined with 0.01 g of HMM polymer in 15 mL tubes. These mixtures were subjected to the same conditions as the kinetic experiment and incubated overnight. Subsequently, the same procedure employed in the adsorption kinetic experiment was followed to prepare samples and quantify the metal ion concentrations.

For sorption measurements, the quantity adsorbed (q_t) was found with the following equation:

$$q_t = \frac{(C_{\rm o} - C_{\rm e}) \times V}{M} \tag{1}$$

where V is the solution's volume (L), M is the adsorbent mass (g), and C_0 and C_e are the initial and equilibrium dye concentrations $(mg L^{-1})$, respectively. Adsorption kinetics were then fit to a pseudo-first-order adsorption model expressed as follows:

$$\log(q_{\rm e} - q_t) = \log q_{\rm e} - \frac{k_1}{2.303}t\tag{2}$$

where q_e (mg g^{-1}) is the amount of dye absorbed onto the sorbent at equilibrium, q_t (mg g⁻¹) is the amount of dye absorbed onto the sorbent at time t (h), and k_1 (g mg⁻¹ h⁻¹) is the pseudo-first-order rate constant. Adsorption isotherms were fit to a Langmuir model expressed as follows:

$$q_{\rm e} = \frac{q_{\rm m} K_{\rm L} C_{\rm e}}{1 + C_{\rm e} K_{\rm L}} \tag{3}$$

where $q_{\rm e}$ (mg g⁻¹) is the amount of dye adsorbed onto the sorbent at equilibrium, $q_{\rm m}$ (mg g⁻¹) is the maximum adsorption capacity of the sorbent at equilibrium, $C_{\rm e}$ (mg L⁻¹) is the equilibrium dye concentration, and $K_{\rm L}$ is the Langmuir equilibrium constant which represents the affinity of sorbent binding sites. The recyclability of HMM carbon sorbents was assessed by determining the equilibration adsorption capacity with a rhodamine b concentration of 400 mg mL⁻¹ followed by thermal treatment to regenerate the sorbent following dye adsorption. Specifically, the sorbent was collected, dried, and exposed to 600 °C under an inert environment for 2 h and repeated for a total of 4 cycles.

Results and discussion

3.1. Fabrication of hierarchically macro-/mesoporous (HMM) polymers

HMM polymers were fabricated by using TPE blends as precursors through two steps including mixing, where varied

loading content of SIS (from 1 to 10 wt%) was introduced to a SEBS matrix, and sulfonation-enabled crosslinking. In this study, SEBS-SIS blends are referred to as SIS-x, where x represents the loading level (wt%) of SIS. Briefly, SEBS-SIS blends were solution cast to establish self-assembled nanostructure through slow solvent evaporation. These TPE blend samples were then submerged in concentrated sulfuric acid at 145 °C to undergo crosslinking. For both TPEs, at elevated temperatures sulfuric acid readily diffuses and reacts with all blocks, including olefinic and polystyrene phases. Specifically, the polystyrene blocks can undergo a sulfonation reaction where sulfonic acid groups are introduced to the aromatic rings preferentially at the para position.26 For polyolefin segments, including poly(ethylene-ran-butylene) and polyisoprene blocks, sulfuric acid reacts with the polymeric backbone and introduces sulfonic acid groups to the polymer chain, which can then undergo homolytic dissociation, producing double bonds within the backbone. Followed by a series of additional reactions, functionalized polyolefins can undergo intermolecular crosslinking through a radical-radical coupling mechanism. Subsequently, SEBS-SIS blends were then washed by DI water to remove residual acid and byproducts, and then dried. It was observed in this work that inclusion of SIS resulted in cleavage of polystyrene blocks from the TPE blend matrix, forming

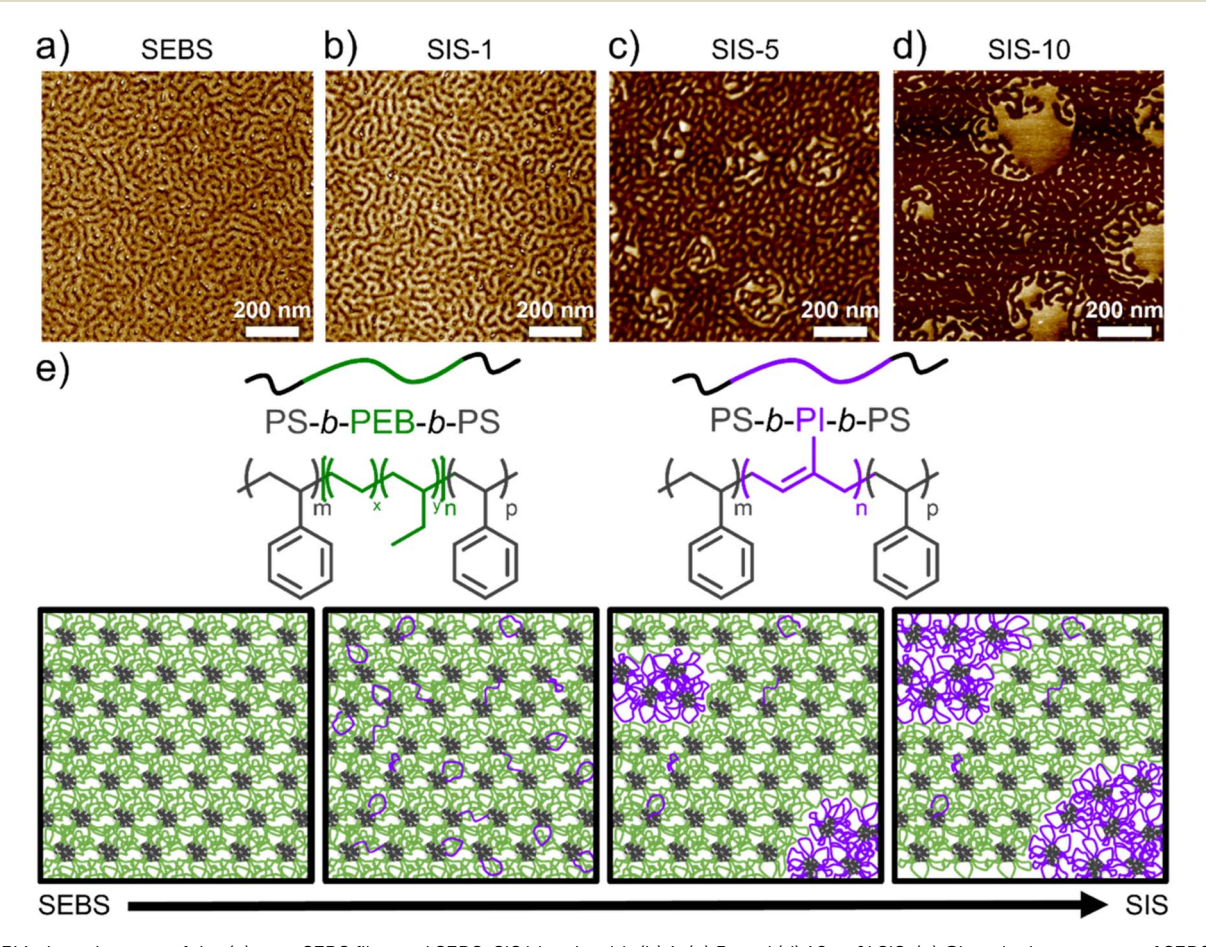


Fig. 1 AFM phase images of the (a) neat SEBS film and SEBS-SIS blends with (b) 1, (c) 5, and (d) 10 wt% SIS. (e) Chemical structures of SEBS and SIS with a schematic demonstrating macrophase separation behavior as a function of SIS concentration.

hierarchically macro-/mesoporous crosslinked polymers. The ability to obtain HMM polymers without a calcination step is highly advantageous due to its lower energy consumption, simplified manufacturing process, and retention of functional groups in the polymer framework, which may be lost upon high temperature treatment from pyrolysis steps.

Bulk SEBS has a cylindrical morphology as shown in AFM image (Fig. 1a), which exhibits minimal change after the addition of 1 wt% SIS (Fig. 1b), indicating efficient mixing between these two TPEs. At greater loadings of SIS (5 and 10 wt%), large spherical features (>100 nm) are observed (Fig. 1c and d), which are associated with macrophase separation between SIS and SEBS, while nanoscale self-assembly of TPEs can also be observed. The macrophase separation between SIS and SEBS has been previously reported, 36,37 driven by the increased interfacial tension due to lack of favorable interaction.³⁸ As shown in Fig. 1, increasing SIS content was observed to increase the size of macro-domains due to further enhanced polymer blend phase separation. Additionally, the maximum roughness depth was observed to increase with higher SIS loading content, shown in Table S1.† The change in TPE-blend morphology from efficient mixing to macrophase separation with increasing SIS loading content is illustrated in Fig. 1e, and these altered polymer blend structures may impact their subsequent sulfonation-enabled crosslinking behaviors.

The progression of sulfonation-induced crosslinking reaction at 145 °C was monitored through FTIR spectra to probe changes in the chemical composition of bulk SEBS and SEBS-SIS blends (Fig. 2a-d). Changes in several characteristic vibrations can be observed, including the bands at 2910 cm⁻¹ and 2850 cm⁻¹ which correspond to alkyl stretching of the polyolefin backbone. This band gradually decreases with increasing reaction time and becomes nearly absent after 3 h for the bulk SEBS, which is in good agreement with a previous report investigating the sulfonation of SEBS.26 In comparison, SIS-1 exhibited an accelerated decay in intensity with alkyl stretching. This enhanced reaction progression is slightly increased with the SIS-5 blend, where the alkyl stretch is nearly absent following 1 h reaction time. This behavior is shown to slightly lessen at even higher loadings, where SIS-10 still exhibits accelerated chemical transformation compared to bulk SEBS, though slower than SIS-1 and SIS-5. These results suggest

potentially enhanced crosslinking kinetics of SEBS-SIS blends in comparison to the bulk SEBS system. We note that alkyl stretching should not completely disappear even in a fully crosslinked sample, while this characteristic peak can become convoluted and hidden from the band corresponding to hydroxyl stretching. Hydroxyl stretching (\sim 3350 cm⁻¹) is rapidly developed within 30 min for all samples, while a band at 1600 cm⁻¹ becomes apparent and increases in intensity with extended reaction times, which is associated with the formation of alkenes in the olefinic backbone, further indicating the progression of crosslinking. With increasing reaction times, bands between 1700 cm⁻¹ and 1600 cm⁻¹ are also observed which suggest side reactions occurred, corresponding to the possible formation of carboxylic acids, ketones, and aldehydes. However, for SEBS-SIS blends with even longer reaction times up to 3 h, these bands convolute once again into a broad peak. Moreover, the introduction of sulfonic acid groups into the polystyrene backbone can be observed with the development of a characteristic band at 1000 cm⁻¹, while their addition to the polyolefin backbone is observed at 1030 cm⁻¹. Interestingly, bulk SEBS shows these two bands retaining significant intensity at longer sulfonation times, whereas the SEBS-SIS blends at early reaction times show a reduced intensity of the peak associated with sulfonic acid groups within the polystyrene backbone. For SEBS-SIS blends, the band at 1000 cm⁻¹ is first observed to decrease in intensity and then merge with band at 1030 cm⁻¹ at longer reaction times. This decrease and subsequent convolution of the band associated with sulfonic acid groups within the polystyrene backbone suggests a decrease in the relative amount of sulfonated polystyrene within SEBS-SIS blends in comparison to the bulk SEBS following sulfonationbased crosslinking. Overall, the chemical structure evolution indicates that the well dispersed and marginally phase separated morphologies can lead to faster reaction kinetics. This reaction kinetics difference may be due to the presence of SIS molecules promoting the crosslinking reaction within SEBS domains. In a previous work, it was found that bulk SEBS required 4 h at 150 °C to fully crosslink, confirmed by FTIR, gel fraction and mass gain, while 90 min is required for bulk SIS at 140 °C;³⁹ here, we observe the inclusion of SIS can potentially improve crosslinking kinetics of TPE blends.

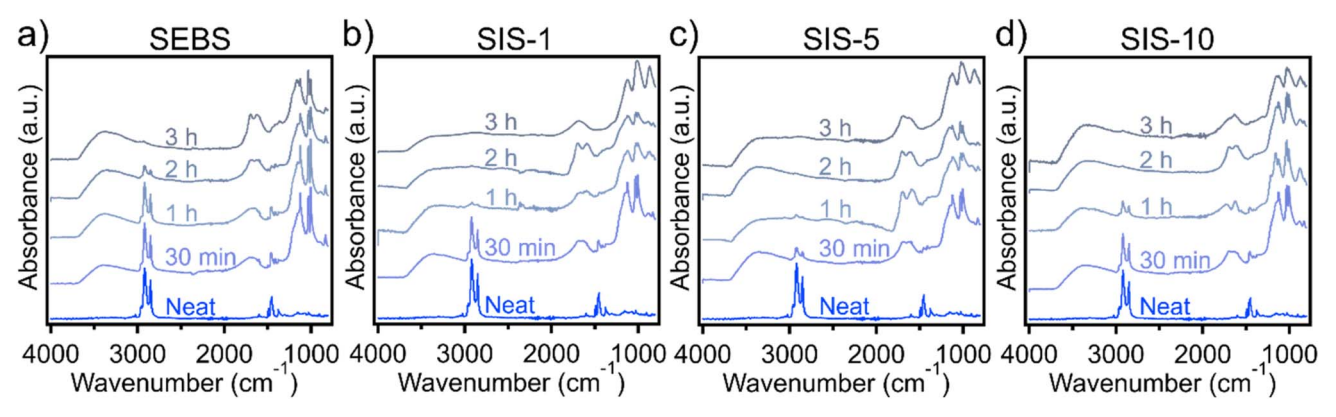


Fig. 2 (a) FTIR spectra as a function of sulfonation time for (a) the bulk SEBS and SEBS-SIS blends with (b) 1, (c) 5, and (d) 10 wt% SIS.

The nanostructure of SEBS-SIS precursors upon blending and sulfonation can be studied through SAXS measurements, as shown in Fig. 3a, where the neat SEBS has a primary ordering peak (q^*) of 0.20 nm⁻¹, corresponding to a domain spacing of 31.4 nm. Additional higher ordering peaks at $\sqrt{3}q^*$ further confirm the presence of hexagonally packed cylindrical morphology in SEBS. For comparison, bulk SIS has a domain spacing of 28.4 nm (Fig. S2†). With 1 wt% SIS loading, the averaged domain spacing decreased slightly to 31.1 nm followed by a further decrease to 30.3 and 29.7 nm for 5 and 10 wt%, respectively, while a slight broadening of the primary peak is also observed. The broadening of the primary peak at higher SIS contents may be due to a slight loss in degree of ordering or convolution of the primary peak from both SEBS and SIS contributions. To assess this, the full width at halfmaxima (FWHM) was determined by fitting the primary scattering peak to a Gaussian model. It was found that the bulk SEBS has a FWHM of 0.035 nm⁻¹ which then increases to 0.064 nm⁻¹ with SIS-1, indicating a slight loss in the degree of ordering following blending. The FWHM of primary scattering peak of SIS-5 and SIS-10 is 0.049 nm⁻¹ and 0.078 nm⁻¹, respectively, indicating their reduced nanostructural ordering compared to the bulk SEBS samples.

To determine how nanostructure is impacted by the sulfonation reaction, SAXS was carried out following 1 h and 2 h of sulfonation time (Fig. 3b and c). The domain spacing of the bulk SEBS increased from 31.4 nm to 35.5 nm and 38.6 nm, after 1 h and 2 h of sulfonation time, respectively. This change is due to both the swelling of polystyrene and polyolefin domains upon reaction.40 With 1 wt% SIS loading, the domain spacing increases from 31.1 nm to 40.3 nm within the first hour of sulfonation-based crosslinking. Following 2 h of reaction time, the domain spacing further increases to 42.2 nm; this indicates the majority of the structural rearrangement occurs within the first hour, which is faster compared to the bulk SEBS. This behavior is also observed for the SIS-5 blend, where domain spacing increases from 30.3 nm to 39.1 nm and 41.6 nm after 1 h and 2 h of reaction time, respectively. Finally, the SIS-10 sample exhibited a similar trend with a domain spacing of 39.1 and 42.2 nm following 1 h and 2 h of sulfonation, respectively. These results suggest that the presence of SIS in the SEBS matrix can play an important role in controlling their morphological evolution. It has been shown in a previous work that sulfonation-induced crosslinking of SIS leads to macropore formation and a complete loss of ordered structures, ³⁹ due to the highly reactive isoprene unit resulting in significant gaseous byproducts released from polymer frameworks. From SAXS results in Fig. 3, it can be observed that mesostructural ordering of all samples in this study can be retained. The slight increase in domain spacing for the SEBS-SIS blends, compared to their SEBS-only counterpart, can be attributed to the portion of SIS that is efficiently mixed slightly expanding the nanostructure.

Following sulfonation-induced crosslinking for 2 h, crosslinked TPE blends were characterized using liquid nitrogen physisorption measurements, which are shown in Fig. 4a. The bulk SEBS, as anticipated, has no presence of mesopores or macropores, however, it is very interesting that a type IV isotherm, indicative of ordered mesoporous materials, is observed for all SEBS-SIS blends. This result suggests the inclusion of SIS results in the removal of styrene blocks within the SEBS majority, leading to the formation of mesopores in the polymer framework. The pore size distributions of these samples are shown in Fig. 4b, which are derived from NLDFT model. It was found that the bulk SEBS has no mesopores, whereas the crosslinked SEBS-SIS blends have pore size distributions centered at 20.9, 21.9, and 20.0 nm for SIS-1, SIS-5, and SIS-10, respectively. Moreover, Fig. 4c shows the resulting pore volume and BET surface areas of different samples, where the bulk SEBS has a very low pore volume of 0.04 cm³ g⁻¹, which increases to 1.12, 0.95, and 0.73 cm 3 g $^{-1}$ for SIS-1, SIS-5, and SIS-10, respectively. The sulfonated SEBS also exhibits a low surface area of 11 m² g⁻¹, which increases to 62, 50, and 44 m² g⁻¹ for SIS-1, SIS-5, and SIS-10, respectively. For HMM polymers derived from SEBS-SIS blends, the decreasing pore volume and surface area with increasing SIS loading level could be attributed to a relative decrease in SEBS content in the blend systems.

To understand how incorporation of SIS leads to mesopore formation, nitrogen physisorption experiments were carried out

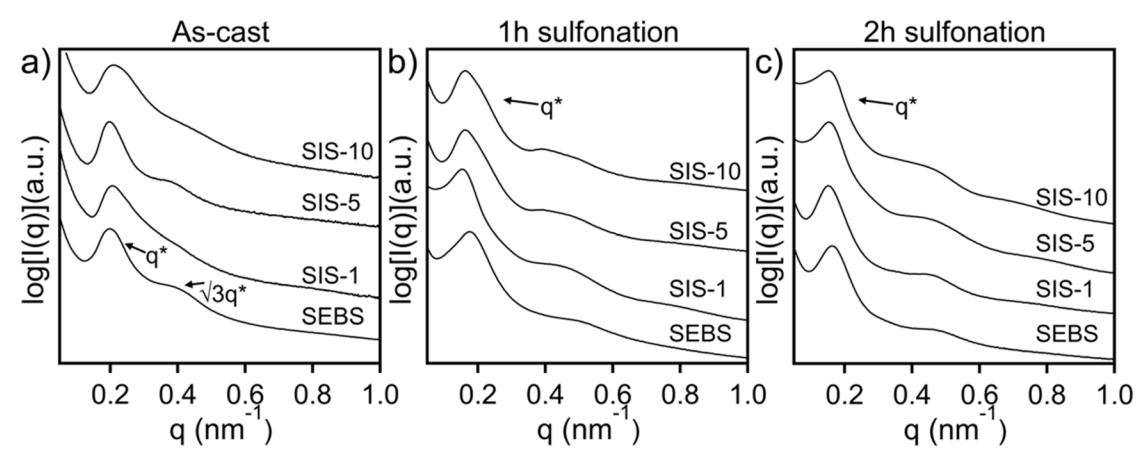


Fig. 3 SAXS profiles for bulk SEBS and SEBS-SIS films (a) as-cast, (b) after 1 h sulfonation and (c) after 2 h sulfonation.

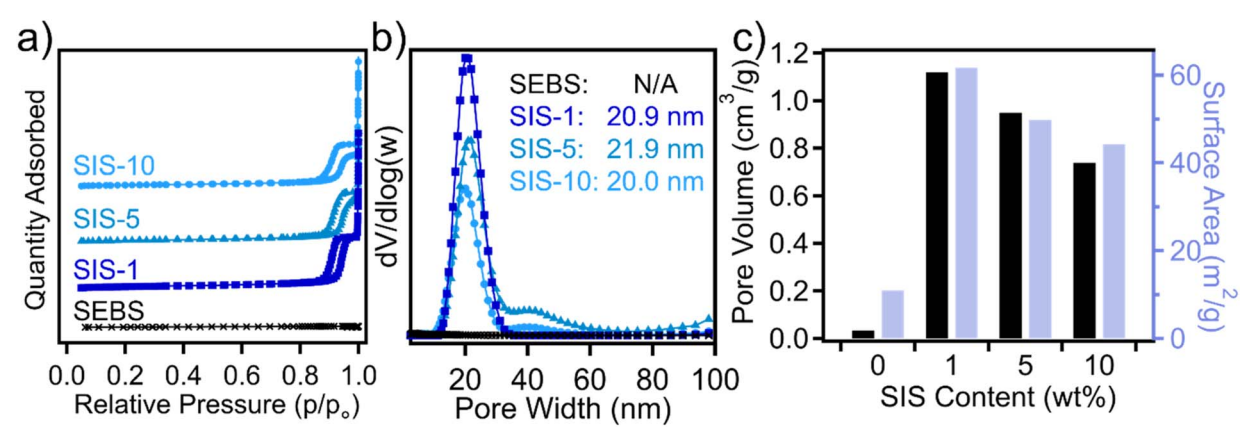


Fig. 4 (a) Liquid nitrogen adsorption isotherms for bulk SEBS and SEBS-SIS blends sulfonated for 2 h, where a type IV isotherm is observed for TPE blend precursors, and (b) associated pore size distributions. For clarity, isotherms were shifted in the Y-direction. (c) Pore volumes and surface areas as a function of SIS loading.

for bulk SEBS and SEBS-SIS blends at various sulfonation reaction times. Fig. 5a displays mesopore volume as a function of sulfonation time, where the bulk SEBS has minimal pore volume for the first few hours, though a slight increase to ~ 0.04 cm³ g⁻¹ is observed following 3 h of reaction time. At much longer reaction times (12 h), no noticeable change is observed (Fig. S3†). The SEBS-SIS blends have no mesopore volume within the first hour of sulfonation, though beginning at 1.5 h mesopore volume increases to 0.41, 0.33, and 0.25 cm³ g⁻¹ for SIS-1, SIS-5, and SIS-10, respectively. Following 3 h of reaction time, mesopore volume appears to plateau with values of 0.40, 0.39, and 0.36 cm 3 g $^{-1}$ for SIS-1, SIS-5, and SIS-10, respectively. The ability to selectively decompose polystyrene domains in TPEs through a sulfonation step is intriguing, as this phenomenon is observed for the first time. Here we note that the removal of polystyrene is primarily attributed to the incorporation of SIS, while the underlying mechanism can be complicated. From literature examples, it is established that degradation of polystyrene to small molecules can occur in various reaction pathways,41-45 some of which involve the use of acid and radicals in the systems. For example, it was shown that

commercial polystyrene can be converted to benzoic acid and benzoyl derivatives under UV light,46 which generate radicals along the polymer chain that then oxidize and generate peroxy radicals that cleave the backbone. This can be further improved with the incorporation of photoinitiators which promote backbone oxidation through hydrogen-atom transfer. Here, we hypothesize the incorporation of highly reactive polyisoprene units coupled with sulfuric acid and elevated temperatures (145 °C) may lead to a similar mechanism, where polyisoprene in the minority phase of TPE-blends undergoes reaction with sulfuric acid generating radical species in the systems. As a result, these radicals following 1.5 h of reaction time selectively degrade polystyrene blocks during the crosslinking of the olefinic phases in the presence of strong acid, resulting in the formation of a crosslinked macro-/mesoporous polymer. To test this hypothesis, a control experiment was carried out where a blend of SEBS with a small amount of homopolymer was prepared, specifically 5 wt% poly(methyl methacrylate) (PMMA; M_w : 38 000 g mol⁻¹). Following sulfonation-based crosslinking at 145 ° C for 1 h, no pore formation is observed through nitrogen physisorption characterization (Fig. S4a†). However, following

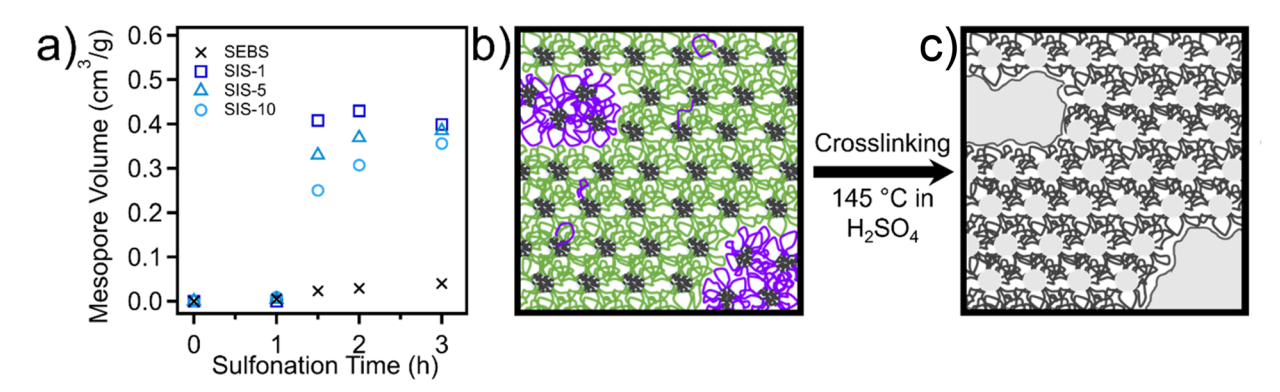


Fig. 5 (a) Pore volume as a function of sulfonation time for bulk SEBS and SEBS-SIS blends, (b) proposed mechanism for removal of polystyrene domains, and (c) schematic illustration of the sulfonation-induced crosslinking reaction resulting in formation of both macropores and mesopores

2 h, a type IV isotherm is once again observed through nitrogen physisorption with a pore size centered at 13.5 nm and a mesopore volume of 0.15 cm3 g-1 (Fig. S4b†). Macropores and mesopores can be visually observed through SEM imaging (Fig. S4c and d†), though compared to SEBS-SIS blends, less macropores are observed within the carbon framework in addition to a reduced ordering in mesopores. The formation of macro-/mesoporous polymer can be directly attributed to the presence of 5 wt% homopolymer, where PMMA undergoes acid hydrolysis during the sulfonation-crosslinking reaction which forms radical species that can facilitate the formation of porous polymer.47 However, the reduction in macro- and mesopore uniformity is due to strong phase separation in the SEBS-PMMA system. In SEBS-SIS system, macropores can derived from the formation of gaseous byproducts that result in more uniform macropore formation. Furthermore, the reduced mesopore volume in the SEBS-PMMA polymer indicates the SEBS-SIS system is more efficient for producing macro-/mesoporous crosslinked polymer. A schematic illustration showing the conversion of SEBS-SIS blends to HMM polymers is provided in Fig. 5b. This result confirms that introducing a small amount of homopolymer that undergoes degradation to form additional radical species during the sulfonation reaction leads to the fabrication of a HMM polymer, enabling the cleavage of polystyrene groups from the polymer backbone and the formation of mesopores.

The hierarchical macro-/mesoporous morphology of the crosslinked polymer was further investigated through SEM imaging in Fig. 6, where the bulk SEBS sample does not exhibit either macropores or mesopores upon sulfonation for 2 h. For the SIS-1 blend, macropores are observed throughout the structure; this could be a result of the efficient mixing of SIS in this composition which results in gaseous byproduct formation and their release creates macropores in the polymer framework. With the SIS-5 and SIS-10 samples, craters are observed on the surface of several micron-size with a diameter of $\sim\!\!4.6~\mu m$ for SIS-5 and $\sim\!\!14.5~\mu m$ for SIS-5, attributed to SIS macrophase separation. Insets are provided to better observe reaction-induced macropores, where SIS-1 has a range of sizes between 220 and 460 nm, SIS-5 has a range between 690 and 900 nm, and

SIS-10 has a range between 1.2 and 2.0 μ m; their formation is attributed to sulfonation reaction, which released gaseous products. These macropore sizes at higher SIS loadings begin to approach values previously reported for bulk SIS following sulfonation (4.3–6.0 μ m). From Fig. 6, an ordered mesoporous morphology with averaged pores size centered at 20.6 nm, 21.7 nm, and 19.6 nm is observed through SEM for SIS-1, SIS-5, and SIS-10, respectively. These SEM imaging results confirm the formation of both macropores and mesopores in these SEBS-SIS blend materials, through a simple and scalable sulfonation reaction process.

3.2. Fabrication of hierarchically macro-/mesoporous carbon

Following sulfonation-induced crosslinking, porous SEBS-SIS blends were then converted to HMM carbons through pyrolysis, specifically through exposure to temperatures up to 800 °C, as shown in Fig. 7a. Fig. 7b indicates bulk carbon yield of different samples as a function of sulfonation time, where SEBS has a gradual increase to 19, 29, and 38% upon 1, 1.5 and 2 h of sulfonation time. A plateau at 42% is reached between 3 to 4 h of reaction time, which is consistent with previous reports.26 For SIS-1 and SIS-5, a plateau at 43% is reached following 1 h of reaction time, where SIS-10 reaches a maximum of 43% following 2 h of sulfonation. Coupling these results with FTIR and SAXS of the crosslinked analogs, it further confirms the introduction of SIS leads to accelerated crosslinking kinetics. Fig. S5† shows TGA thermograms of bulk SEBS and SEBS-SIS blends sulfonated for 4 h under nitrogen environment upon 800 °C, where the bulk SEBS has a residual mass of approximately 52%. We note that bulk SIS was previously reported to have a carbon yield of 35 wt% following sulfonation-based crosslinking.39 These results confirm that these crosslinked SEBS-SIS blends have a relatively limited compositional impact on their final carbon yield.

Nanostructure of carbons derived in our system was investigated through SAXS measurements as shown in Fig. 7c, where for a bulk SEBS sulfonated for 1 h, there is no clear primary ordering peak, indicating insufficient crosslinking conditions

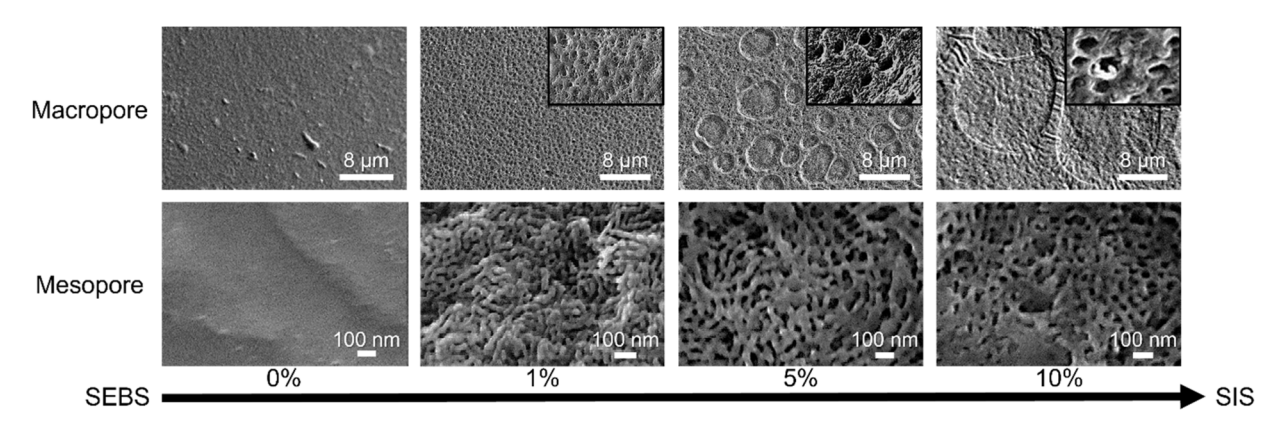


Fig. 6 SEM micrographs of bulk SEBS and SEBS-SIS blends sulfonated for 2 h, indicating dual macroporous and mesoporous regimes, with inset images confirming the presence of macropores (inset heights: 5.9 μm, inset lengths: 8.9 μm).

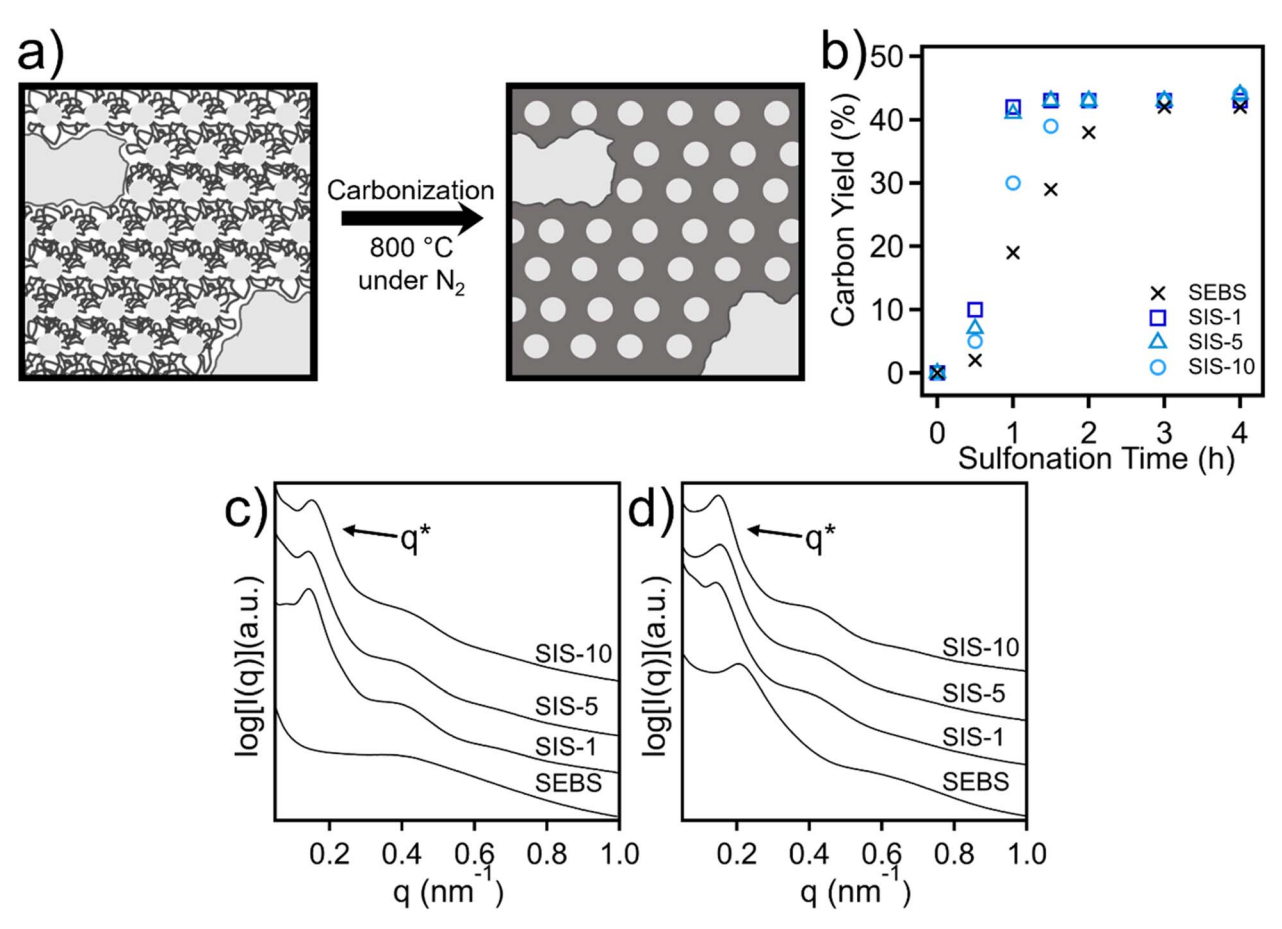


Fig. 7 (a) Schematic illustration of pyrolysis under inert environment to produce HMM carbons. (b) Carbon yield as a function of sulfonation time for bulk SEBS and SEBS-SIS blends. SAXS profiles for (c) 1 h sulfonated and (d) 2 h sulfonated bulk SEBS and SEBS-SIS blends following carbonization

that result in complete nanostructure collapse during carbonization. This disruption of ordered nanostructure is not observed for the SEBS-SIS blends (sulfonated for 1 h), which have a pronounced primary ordering peak with domain spacings of 35.1, 35.5, and 33.8 nm for SIS-1, SIS-5, and SIS-10, respectively. Following carbonization of samples sulfonated for 2 h, SAXS results in Fig. 7d show nanostructure retention of the bulk SEBS with a domain spacing of 30.7 nm, however this value is lower than expected for a sufficiently crosslinked sample. With longer sulfonation reaction times up to 4 h, bulk SEBS carbon domain spacings reach 34.2 nm, which is consistent with previous reports for a fully crosslinked SEBS (Fig. S6†).26

Similar to the HMM polymer analogs, a dual macro-/ mesoporous morphology can be observed through SEM imaging in Fig. 8 for carbonized SEBS-SIS blends with a sulfonation time of 2 h. The bulk SEBS shows no macropores and a mesoporous morphology can be observed with an averaged pore size of 19.6 nm. For SIS-1, SIS-5, and SIS-10 derived carbons, macropores are observed to be retained following carbonization; their sizes are consistent between blend compositions for the carbons (with a broad range between 65 and 160 nm, broadly centered at ~100 nm). The averaged

mesopore size of SIS-1, SIS-5, and SIS-10 derived carbons is approximately 18.2 nm, 18.6 nm, and 16.9 nm, respectively. The mesopore shrinkage may be attributed to the increased amount of macropores in the system, leading to a further weakened carbon framework. These results confirm the successful preparation of HMM carbons through this facile two-step sulfonation-based crosslinking and direct pyrolysis approach.

Pore textures of SEBS-SIS blend-derived HMM carbons with varied precursor compositions were determined through nitrogen physisorption experiments to assess changes in porosity, pore size distributions, and BET surface areas. Fig. 9a shows the nitrogen adsorption isotherms for porous carbons derived from bulk SEBS and the SEBS-SIS blends. Pore size distributions are shown in Fig. 9b, where the bulk SEBS exhibits a pore size distribution centered at 19.2 nm, compared to 18.3 nm, 18.3 nm, 16.1 nm for SIS-1, SIS-5, and SIS-10 derived carbons, respectively. The slight decrease in pore size for the blends can be attributed to a weakened carbon framework from macropore presence leading to increased shrinkage. Furthermore, a similar, marginal shoulder is observed at higher pore sizes around 40 nm, though this is predominantly observed for SIS-5. The mesopore volumes and BET surface areas are shown in Fig. 9c, where the bulk SEBS has a pore volume of 0.11 cm³

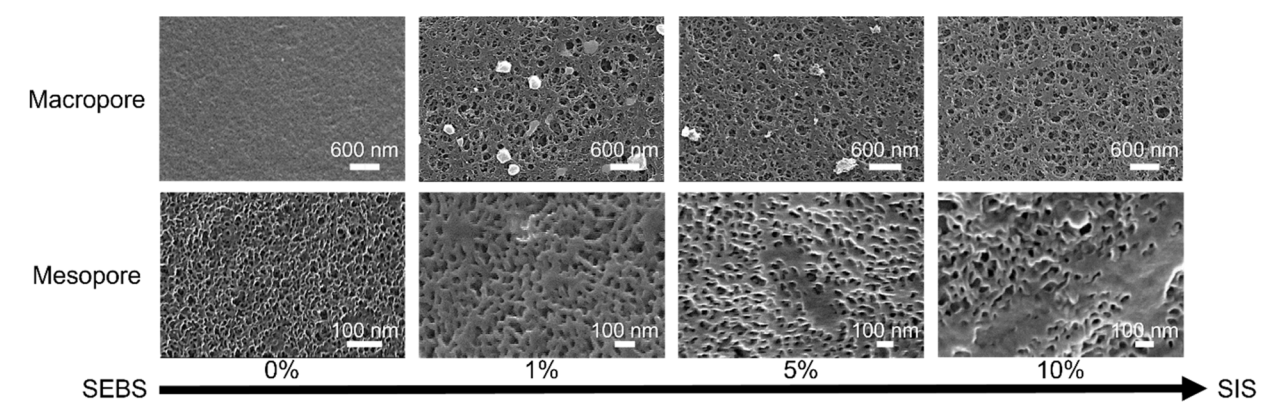


Fig. 8 SEM micrographs of carbonized SEBS and SEBS-SIS blends, indicating retention of dual macroporous and mesoporous regimes following

 g^{-1} and surface area of 61 m² g^{-1} . This is significantly lower than a sufficiently crosslinked carbon precursor with 4 h of sulfonation time, which exhibits a pore volume of 0.41 cm³ g⁻¹ and a surface area of 356 $\mathrm{m}^2~\mathrm{g}^{-1}$. A mesopore volume of 0.83 $cm^3 g^{-1}$, 0.55 $cm^3 g^{-1}$, and 0.46 $cm^3 g^{-1}$ is observed for carbons derived from SIS-1, SIS-5, and SIS-10 precursors with a sulfonation time of 2 h, respectively. These results indicate that pore volumes exceeding the maximum observed for bulk SEBSderived OMCs can be achieved by introducing low amounts of SIS, however these values begin to decrease and approach bulk SEBS at high SIS loading levels. A similar behavior is observed with surface area, with SIS-1, SIS-5, and SIS-10 derived HMM carbons exhibiting surface areas 529, 534, and 478 m² g⁻¹, respectively. These surface area values are comparable to other HMM carbons prepared through several dual templating approaches. 11,48-50 Additionally, our process to prepare HMM carbons results in the incorporation of sulfur heteroatoms that are retained following conversion to carbon as shown in XPS results in Fig. S7.† The SEBS control exhibits a sulfur content of 1.1 at%, whereas the 1, 5, and 10 wt% blends exhibit a doping of 0.5, 0.6, and 0.6 at%, respectively. These values are consistent with previous reports,26 in which the introduction of sulfur

heteroatoms into carbon sorbents may lead to altered interactions between guest molecules and carbon surface.51 This simple, two-step process of crosslinking and carbonization using commodity thermoplastic elastomers as precursors is cost-effective and resource-efficient, providing a significant advantage for scaled manufacturing of HMM carbons.

The versatility of this HMM carbon fabrication method was demonstrated by extending to additional SEBS samples with different molecular weights, including 89 000 g mol⁻¹ (SEBS-89) and 100 000 g mol⁻¹ (SEBS-100), allowing control over mesopore size through varying precursor identity. These two precursors were respectively blended with 5 wt% SIS, following a similar reaction procedure as described in previous sections (i.e. 2 h sulfonation at 145 °C). Their chemical composition is also provided in the Experimental section. The SAXS profile of HMM carbon derived from SEBS-89 exhibited a lower domain spacing of 24.3 nm, compared to 30.7 nm of the model SEBS system (Fig. 10a), while an increase in the degree of ordering was observed. The liquid nitrogen physisorption measurements (Fig. 10b and c) show a uniform pore size distribution centered at 12.9 nm, further confirming the smaller pore size obtained from using a lower molecular weight SEBS precursor, with

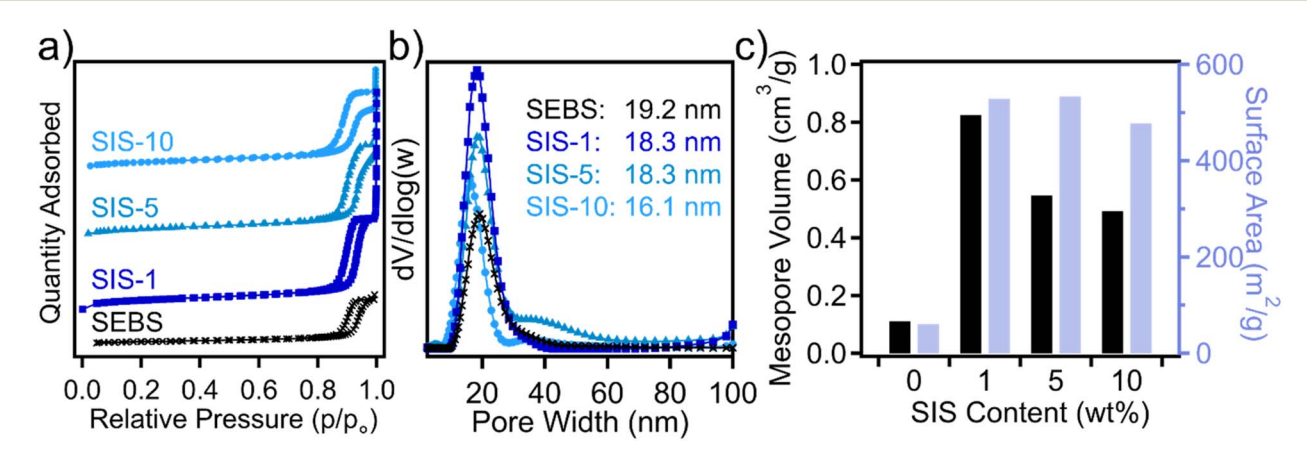


Fig. 9 (a) Nitrogen adsorption isotherms for carbonized bulk SEBS and SEBS-SIS blends, where a type IV isotherm is observed, and (b) associated pore size distributions. For clarity, isotherms were shifted in the Y-direction. (c) Mesopore volumes and surface areas as a function of SIS loading.

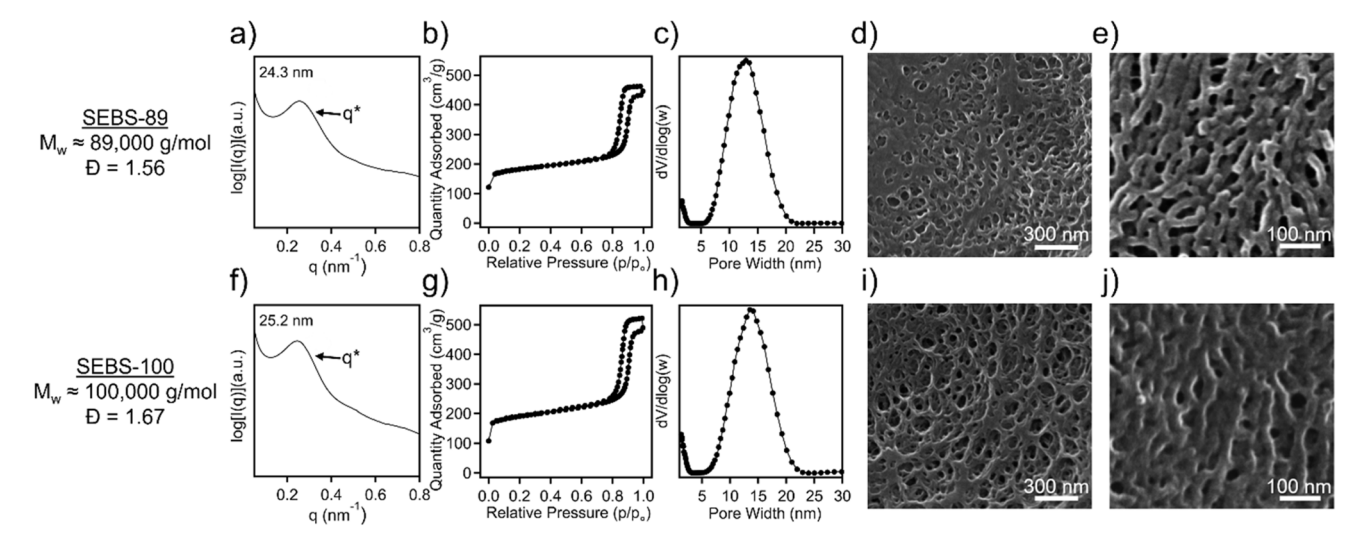


Fig. 10 (a) SAXS profile, (b) nitrogen adsorption isotherm, (c) corresponding pore size distribution, SEM micrographs of (d) mesopore and (e) macropore regimes for the SEBS-89 precursor. (f) SAXS profile, (g) nitrogen adsorption isotherm, (h) corresponding pore size distribution, SEM micrographs of (i) mesopore and (j) macropore regimes for the SEBS-100 precursor.

a pore volume of 0.67 cm³ g⁻¹ and a BET surface area of 500 m² g⁻¹, significantly greater than the 216 m² g⁻¹ previously reported for the bulk SEBS-89 precursor.26 Additionally, a dual macro-/mesopore morphology can be observed through SEM imaging (Fig. 10d and e). The broad generalizability of this synthetic strategy is further demonstrated with a SEBS-100 precursor, where the formation of HMM carbons with wellordered mesopore morphologies are confirmed through SAXS (Fig. 10f); this material has an averaged domain spacing of 25.2 nm, pore size (Fig. 10g and h) centered around 13.5 nm, a pore volume of 0.84 cm³ g⁻¹, and surface area of 526 m² g⁻¹. Furthermore, the nitrogen adsorption isotherm and pore size distribution of SEBS-89 and SEBS-100 suggest the presence of micropores. To better assess their microporous characteristics, carbon dioxide physisorption measurements were conducted and micropore size distributions were extracted with NLDFT modeling. The CO₂ adsorption isotherms are shown in Fig. S8[†] for both SEBS-89 and SEBS-100. The combined pore size distributions determined from CO2 and N2 isotherms display the dual micro- and mesoporous regimes of SEBS-89 and SEBS-100 (Fig. S9†). As shown in Fig. 10i and j, SEM imaging confirms the presence of macropores with a range of 50-110 nm and ordered mesopores in derived carbon samples. With tailorable mesopore textures controlled through precursor selection, the broad applicability and robustness of this synthetic route is demonstrated toward attaining different HMM materials with altered hierarchical morphology.

3.3. Application of HMM materials as sorbents for water remediation

An important application of HMM polymers is their use as sorbents for water remediation, where the removal of toxic heavy metal ions from aqueous environments has been demonstrated with various polymeric systems. 52-57 To demonstrate the practical application of TPE blend-derived HMM

polymers, adsorption studies were carried out with two model compounds, including Co²⁺ and Ni²⁺. Specifically, the SIS-5 HMM polymer was selected for investigating adsorption kinetics for the two metal ions through monitoring the change in metal ion concentration over contact time, starting with an initial concentration of 12 mg L^{-1} . Fig. 11a and b show that SIS-5 HMM polymer achieved adsorption equilibrium for Co²⁺ and Ni²⁺ within only 20 minutes, accompanied by significantly high removal rates for Co2+ and Ni2+ (95.3% and 92.9%, respectively), which surpass efficiencies reported in many previous studies.58-61 The adsorbed concentrations of Co2+ and Ni2+ reached 5.96 and 5.87 mg g⁻¹, respectively, despite their low initial concentrations, suggesting rapid kinetics and strong affinity of our HMM polymer for heavy metal ions. The adsorption isotherms of HMM polymer for both Co²⁺ and Ni²⁺ fit well with the Langmuir model as observed in Fig. 11c, where Co^{2+} exhibited a maximum adsorption capacity (q_{m}) of 49.7 mg g^{-1} and a Langmuir equilibrium constant (K_L) of 0.192 L mg⁻¹, while Ni $^{2+}$ showed a $q_{\rm m}$ of 74.9 mg g $^{-1}$ and a $K_{\rm L}$ of 8.42 imes 10 $^{-3}$ L mg⁻¹ (Table S2†). These parameters are comparable to or better than the values reported for other polymers as shown in Tables S3 and S4.† (ref. 59-67) Specifically, in terms of Co²⁺ adsorption, our HMM polymer exhibited both $q_{\rm m}$ and $K_{\rm L}$ values that rank among the highest compared to those reported in other studies. $^{59-61,63-67}$ For instance, the $q_{
m m}$ of our polymer is approximately 14 times higher than that of an anthranilic acid - 2aminopyridine - formaldehyde terpolymer, 64 and the $K_{\rm L}$ is about 7 times higher than that of a mesoporous silicasupported polyethyleneimine.60 Notably, the adsorption of Co²⁺ on our HMM polymer reached equilibrium in just 20 minutes, 3-15 times faster than other polymers listed in Table S3,† suggesting the fast kinetics of Co²⁺ adsorption on the HMM polymer, which is crucial for applications in flow-through columns designed for removing metals from water. Regarding $\mathrm{Ni}^{2^{+}}$ adsorption, despite exhibiting a relatively small K_{L} value, it

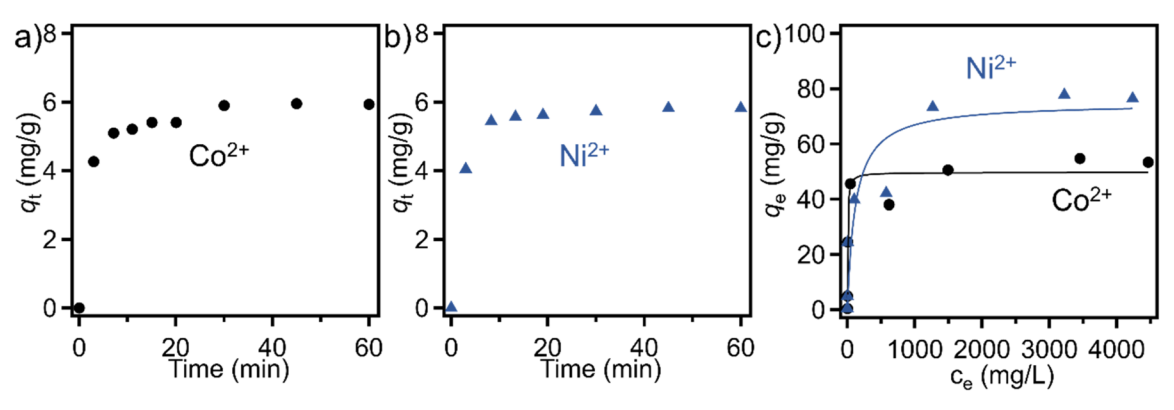


Fig. 11 (a) Co^{2+} adsorption as a function of contact time at an initial metal ion concentration of 12 mg L^{-1} . (b) Ni^{2+} adsorption as a function of contact time at an initial metal ion concentration of 12 mg L^{-1} . (c) Co^{2+} and Ni^{2+} adsorption isotherms fit with a Langmuir isotherm model for HMM polymers.

still reached equilibrium in less than 20 minutes, faster than most other studies. ^{59,62,64,66,67} Collectively, these findings provide fundamental insights into the properties of our HMM polymer for metal ion adsorption, while highlighting their potential for metal removal applications. We also note that our method for preparing HMM polymers employed cost-effective commodity plastics as the starting materials, in conjugation with a simple sulfonation steps, which can provide high scalability to address practical applications.

Following the implementation of HMM polymers as heavy metal capture agents, we next assessed the application of HMM carbons. HMM carbons have been shown in several works to have great promise for the adsorption of organic pollutants from water streams.5,7,68,69 To show the versatility of HMM materials within water remediation applications, dye adsorption experiments were performed with a water-soluble dye, rhodamine b, as a model system. Specifically, the SEBS-89 precursor with 5 wt% SIS was selected and compared to an OMC control derived from the same precursor (prepared with the absence of SIS polymer). Adsorption kinetics were first assessed by investigating the adsorption capacity as a function of contact time for a concentration of 50 mg L⁻¹ (Fig. 12a). The HMM carbon exhibited enhanced adsorption kinetics and a higher equilibrated adsorption capacity (98 mg g^{-1}) in comparison to the OMC control (51 mg g^{-1}). The adsorption kinetics results were then fit to a pseudo first-order

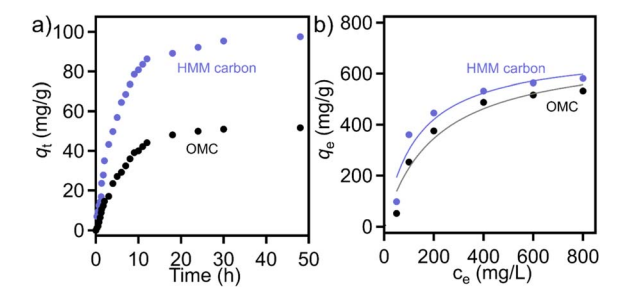


Fig. 12 (a) Dye adsorption as a function of contact time at a concentration of 50 mg mL $^{-1}$ and (b) adsorption isotherms between 50 and 800 mg mL $^{-1}$ fit with a Langmuir isotherm model for 5% SIS blend-derived HMM carbon and an OMC derived from SEBS-89.

model (Fig. S10†) and displayed good accordance with both the control ($q_{\text{e.cal}} = 52.8$, $R^2 = 0.995$) and the HMM carbon ($q_{\text{e.cal}} =$ 96.0, $R^2 = 0.998$). The rate constant of the HMM carbon (1.982) h⁻¹) at the 50 mg mL⁻¹ concentration was also higher than the OMC control (1.723 h^{-1}) , where the enhanced pore accessibility and mass transport associated with the introduction of macropores lead to improved sorption performance. A previous study shows that an ordered mesoporous carbon prepared through a conventional soft-templating approach,70 followed by doping with cobalt, resulted in slightly higher adsorption capacity (151.7 mg g^{-1}) and rate constant (0.15 h^{-1}) when assessed with a pseudo first-order model at a rhodamine b concentration of 50 mg mL⁻¹. The slightly higher sorbent performance in their work could be a result of the higher surface area (955 m² g⁻¹) and/ or the high cobalt loading (8.9 at%) leading to enhanced dye interactions. Adsorption isotherms were carried out for various dye concentrations (in the range of 50-800 mg mL⁻¹) to determine equilibrium adsorption capacities (Fig. 12b), which were fit to a Langmuir isotherm model. The HMM carbon exhibits higher adsorption capacities compared to the OMC control at all dye concentrations with an experimental maximum value of 581 and $533~{
m mg~g^{-1}}$ for the HMM carbon and OMC control, respectively. The Langmuir constant for the HMM carbon (0.012 L mg⁻¹) is higher than the control (0.006 $L\ mg^{-1}$), while both have comparable q_{max} values (637 to 641 mg g⁻¹, respectively). The performance of HMM materials against pollutants for water remediation demonstrate how introducing macropores into the OMC matrix leads to sorbent performance enhancement.

To assess the recyclability of the adsorbent, cycling studies were performed with the model HMM carbon and rhodamine b dye at a concentration of 400 mg mL⁻¹. Following determination of equilibration adsorption capacities, a thermal treatment step was performed similar to previous studies to decompose adsorbed dyes and regenerate adsorbents.⁷¹ Specifically, adsorbents were collected, dried, and exposed to 600 °C under an inert environment for 2 h. This process was repeated for 4 cycles, shown in Table S5,† where the adsorption capacity was observed to decrease to 40% after the 2nd cycle, 37% after the 3rd cycle, and 35% after the 4th cycle, all compared to their first-cycle performance. Following the 4th

cycle, nitrogen physisorption measurements were conducted on the regenerated sorbent to examine potential changes in pore textures (Fig. S11†). Compared to the initial carbon (surface area: 500 m² g⁻¹ and pore volume: 0.67 cm³ g⁻¹), the regenerated carbon has a slightly reduced surface area (467 m² g⁻¹) and pore volume (0.53 cm³ g⁻¹) though it is mostly retained following 3 cycles of dye adsorption and regeneration. The decreased pore textures can be attributed to dye decomposition resulting in slight amounts of deposition onto the carbon surface. The reduced adsorption capacities of HMM carbon following cycling tests can be attributed to a combination of reduced accessible pore areas and a change in the carbon surface functionalities following initial cycle of dye adsorption and thermal decomposition. Specifically, high temperature thermal destruction of adsorbed rhodamine b within confined pores may lead to re-deposition of decomposed byproducts into the pore surface, and thus alter the sorbent-sorbate interactions. While further research opportunities exist to advance the cyclability of these HMM carbon sorbents through understanding the change in pore textures as a function of recycling events, as well as development more efficient desorption methods, we note that the recycling efficiencies of our materials are comparable to porous carbons from several studies.72-74

Conclusions

To unlock the full potential of hierarchically macro-/ mesoporous (HMM) materials, a simple and scalable synthetic strategy is needed to facilitate their scaled production. In this work, we report the conversion of commodity thermoplastic elastomer blends to produce HMM materials, enabled by sulfonation-induced crosslinking. The incorporation of isoprene units was found to facilitate the selectively cleavage of polystyrene domains with the presence of acid, leading to the fabrication of HMM polymers with a uniform pore size distribution of mesopores. Moreover, low amounts of SIS content can accelerate crosslinking kinetics. Following exposure to elevated temperatures for pyrolysis, HMM carbons can be prepared with ordered mesopore structures. Furthermore, the broad applicability of this approach is demonstrated through extension to two additional commercial TPE systems, indicating the generalizability of this synthetic platform. Moreover, we demonstrate that the TPE blend-derived HMM materials can be employed as high-performance sorbents for the efficient removal of heavy metal ions and organic pollutants from aqueous systems. This work provides a streamlined and innovative method for the preparation of porous materials containing distinct pore sizes and tailorable morphologies.

Conflicts of interest

There are no conflicts to declare.

Acknowledgements

This project was supported by National Science Foundation under grant #CMMI-2239408 and in part by NSF grant #1757220. The authors would like to acknowledge Dr Derek Patton and Jeff Aguinaga for assistance with XPS experiments. This research was supported in part by a Major Research Instrumentation grant from the National Science Foundation Award (DMR-1726901). Guorong Ma and Xiaodan Gu acknowledge NSF funding No. CHE-2304969 for supporting the scattering characterization of polymers.

References

- 1 Z. Meng, N. Chen, S. Cai, R. Wang, W. Guo and H. Tang, Int. J. Energy Res., 2021, 45, 6250-6261.
- 2 W. Kou, Y. Zhang, J. Dong, C. Mu and L. Xu, ACS Appl. Energy Mater., 2020, 3, 1875-1882.
- 3 C. M. A. Parlett, K. Wilson and A. F. Lee, Chem. Soc. Rev., 2013, 42, 3876-3893.
- 4 P. Trogadas, V. Ramani, P. Strasser, T. F. Fuller and M. O. Coppens, Angew. Chem., Int. Ed., 2016, 55, 122-148.
- 5 G. Tao, L. Zhang, Z. Hua, Y. Chen, L. Guo, J. Zhang, Z. Shu, J. Gao, H. Chen, W. Wu, Z. Liu and J. Shi, Carbon, 2014, 66, 547-559.
- 6 T. Y. Ma, X. J. Zhang and Z. Y. Yuan, J. Phys. Chem. C, 2009, 113, 12854-12862.
- 7 S. Qiu, B. Jiang, X. Zheng, J. Zheng, C. Zhu and M. Wu, Carbon, 2015, 84, 551-559.
- 8 Y. N. Wu, B. Zhang, F. Li, W. Zhu, D. Xu, P. Hannam and G. Li, J. Mater. Chem., 2012, 22, 5089-5097.
- 9 P. Han, S. H. Chung and A. Manthiram, Small, 2019, 15, 1900690.
- 10 A. Chen, Y. Yu, Y. Li, Y. Wang, Y. Li, S. Li and K. Xia, J. Mater. Sci., 2016, 51, 4601-4608.
- 11 X. Guo, B. Sun, J. Zhang, H. Liu and G. Wang, J. Mater. Chem. A, 2016, 4, 9774-9780.
- 12 M. H. Sun, S. Z. Huang, L. H. Chen, Y. Li, X. Y. Yang, Z. Y. Yuan and B. L. Su, Chem. Soc. Rev., 2016, 45, 3479-3563.
- 13 Z. Sun, Y. Deng, J. Wei, D. Gu, B. Tu and D. Zhao, Chem. Mater., 2011, 23, 2176-2184.
- 14 M. Kozakiewicz-Latała, D. Marciniak, K. Krajewska, A. Złocińska, K. Prusik, B. Karolewicz, K. P. Nartowski and W. Pudło, Mol. Pharm., 2023, 20, 641-649.
- 15 X. Li, D. Han, T. Guo, J. Peng, L. Xu and M. Zhai, Ind. Eng. Chem. Res., 2018, 57, 13511-13518.
- 16 Z. Y. Yuan and B. L. Su, J. Mater. Chem., 2006, 16, 663-677.
- 17 S. Dutta, A. Bhaumik and K. C. W. Wu, Energy Environ. Sci., 2014, 7, 3574-3592.
- 18 H. F. Fei, Y. Long, H. J. Yu, B. M. Yavitt, W. Fan, A. Ribbe and J. J. Watkins, ACS Appl. Mater. Interfaces, 2020, 12, 57322-
- 19 H. F. Fei, W. Li, S. Nuguri, H. J. Yu, B. M. Yavitt, W. Fan and J. J. Watkins, Chem. Mater., 2020, 32, 6055-6061.
- 20 B. Fang, J. H. Kim, M. S. Kim and J. S. Yu, Acc. Chem. Res., 2013, 46, 1397-1406.
- 21 X. Y. Yang, L. H. Chen, Y. Li, J. C. Rooke, C. Sanchez and B. L. Su, Chem. Soc. Rev., 2017, 46, 481-558.
- 22 R. T. Woodward, D. W. H. Fam, D. B. Anthony, J. Hong, T. O. McDonald, C. Petit, M. S. P. Shaffer and A. Bismarck, Carbon, 2016, 101, 253-260.

- 23 Y. Zhang, Y. Chen, Y. Shen, Y. Yan, J. Pan, W. Shi and L. Yu, *Chempluschem*, 2016, **81**, 108–118.
- 24 C. T. Nguyen and D. P. Kim, *J. Mater. Chem.*, 2011, **21**, 14226–14230.
- 25 Z. Zhou, T. Liu, A. U. Khan and G. Liu, *Sci. Adv.*, 2019, 5(2), eaau6852.
- 26 M. Robertson, A. Guillen-Obando, A. Barbour, P. Smith, A. Griffin and Z. Qiang, *Nat. Commun.*, 2023, **141**, 1–11.
- 27 M. Kopeć, M. Lamson, R. Yuan, C. Tang, M. Kruk, M. Zhong, K. Matyjaszewski and T. Kowalewski, *Prog. Polym. Sci.*, 2019, 92, 89–134.
- 28 D. Wu, F. Xu, B. Sun, R. Fu, H. He and K. Matyjaszewski, *Chem. Rev.*, 2012, **112**, 3959–4015.
- 29 G. Zhang, C. Ni, L. Liu, G. Zhao, F. Fina and J. T. S. Irvine, *J. Mater. Chem. A*, 2015, 3, 15413–15419.
- 30 G. Chen, Y. Yan, J. Wang, Y. S. Ok, G. Zhong, B. Y. Guan and Y. Yamauchi, *Angew. Chem., Int. Ed.*, 2020, **59**, 19663–19668.
- 31 M. Seo, S. Kim, J. Oh, S. J. Kim and M. A. Hillmyer, *J. Am. Chem. Soc.*, 2015, **137**, 600–603.
- 32 M. Robertson, A. Griffin, A. G. Obando, A. Barbour, R. Davis and Z. Qiang, *Mol. Syst. Des. Eng.*, 2023, **8**, 1156–1164.
- 33 A. Griffin, G. Chen, M. Robertson, K. Wang, Y. Xiang and Z. Qiang, ACS Omega, 2023, 8, 15781–15789.
- 34 T. Shi, Z. Song, Y. Lv, D. Zhu, L. Miao, L. Gan and M. Liu, *Chin. Chem. Lett.*, 2024, 109559.
- 35 C. Hu, Y. Qin, Z. Song, P. Liu, L. Miao, H. Duan, Y. Lv, L. Xie, M. Liu and L. Gan, J. Colloid Interface Sci., 2024, 658, 856– 864.
- 36 S. Jangareddy, T. Sun, A. B. Burns and R. A. Register, *Macromolecules*, 2021, 54, 3999–4009.
- 37 X. Zhang, H. Chen, T. Tang and B. Huang, *Macromol. Chem. Phys.*, 1995, 196, 3585–3595.
- 38 S. Jangareddy and R. A. Register, *Macromolecules*, 2020, 53, 9142–9151.
- 39 A. Guillen Obando, M. Robertson, P. Smith, S. Jha, D. L. Patton and Z. Qiang, New J. Chem., 2022, 2219–2228.
- 40 M. Robertson, A. Barbour, A. Griffin, A. G. Obando, P. Smith and Z. Qiang, ACS Appl. Eng. Mater., 2023, 1, 2577–2588.
- 41 N. Grassie and N. A. Weir, *J. Appl. Polym. Sci.*, 1965, **9**, 975–986.
- 42 T. R. Price and R. B. Fox, *J. Polym. Sci., Part B: Polym. Lett.*, 1966, 4, 771–774.
- 43 J. F. Rabek and B. Ranby, J. Polym. Sci., Polym. Chem. Ed., 1974, 12, 273–294.
- 44 B. Mailhot and J. L. Gardette, Macromolecules, 1992, 25, 4119-4126.
- 45 H. Kaczmarek, A. Kamińska, M. Światek and S. Sanyal, *Eur. Polym. J.*, 2000, **36**, 1167–1173.
- 46 S. Oh and E. E. Stache, J. Am. Chem. Soc., 2022, 144, 5745-5749.
- 47 J. Semen and J. B. Lando, *Macromolecules*, 1969, 2, 570–575.
- 48 Y. Deng, C. Liu, T. Yu, F. Liu, F. Zhang, Y. Wan, L. Zhang, C. Wang, B. Tu, P. A. Webley, H. Wang and D. Zhao, *Chem. Mater.*, 2007, 19, 3271–3277.

- 49 J. Sun, D. Ma, H. Zhang, X. Bao, G. Weinberg and D. Su, *Microporous Mesoporous Mater.*, 2007, **100**, 356–360.
- 50 T. Sun, L. Xu, S. Li, W. Chai, Y. Huang, Y. Yan and J. Chen, *Appl. Catal.*, *B*, 2016, **193**, 1–8.
- 51 M. Robertson, A. G. Obando, B. Nunez, H. Chen and Z. Qiang, ACS Appl. Eng. Mater., 2022, 1, 165–174.
- 52 Y. Zhang, J. R. Vallin, J. K. Sahoo, F. Gao, B. W. Boudouris, M. J. Webber and W. A. Phillip, ACS Cent. Sci., 2018, 4, 1697–1707.
- 53 R. Zowada and R. Foudazi, *ACS Appl. Polym. Mater.*, 2019, **1**, 1006–1014.
- 54 H. Demey, T. Vincent and E. Guibal, *Chem. Eng. J.*, 2018, **332**, 582–595.
- 55 Z. A. Chaleshtari and R. Foudazi, *ACS Appl. Polym. Mater.*, 2020, 2, 3196–3204.
- 56 V. Beaugeard, J. Muller, A. Graillot, X. Ding, J. J. Robin and S. Monge, *React. Funct. Polym.*, 2020, **152**, 104599.
- 57 M. Gomez-Suarez, Y. Chen and J. Zhang, *Polym. Chem.*, 2023, 14, 4000–4032.
- 58 Z. Zhou, D. Kong, H. Zhu, N. Wang, Z. Wang, Q. Wang, W. Liu, Q. Li, W. Zhang and Z. Ren, *J. Hazard. Mater.*, 2018, 341, 355–364.
- 59 N. Samadi, R. Hasanzadeh and M. Rasad, J. Appl. Polym. Sci., 2014, 132, 41642.
- 60 Y. Liu, Z. Liu, J. Dai, J. Gao, J. Xie and Y. Yan, *Chin. J. Chem.*, 2011, 29, 387–398.
- 61 A. Masoumi, M. Ghaemy and A. N. Bakht, *Ind. Eng. Chem. Res.*, 2014, 53, 8188–8197.
- 62 D. F. Apopei, M. V. Dinu, A. W. Trochimczuk and E. S. Dragan, *Ind. Eng. Chem. Res.*, 2012, **51**, 10462–10471.
- 63 A. Masoumi and M. Ghaemy, *Carbohydr. Polym.*, 2014, **108**, 206–215.
- 64 R. S. Azarudeen, R. Subha, D. Jeyakumar and A. R. Burkanudeen, *Sep. Purif. Technol.*, 2013, **116**, 366–377.
- 65 R. Kang, L. Qiu, L. Fang, R. Yu, Y. Chen, X. Lu and X. Luo, *J. Environ. Chem. Eng.*, 2016, 4, 2268–2277.
- 66 Z. Lin, Y. Zhang, Y. Chen and H. Qian, Chem. Eng. J., 2012, 200–202, 104–112.
- 67 P. Sun, W. Zhang, B. Zou, X. Wang, L. Zhou, Z. Ye and Q. Zhao, *Appl. Clay Sci.*, 2021, 209, 106151.
- 68 J. Wang, Y. Wang, Y. Liang, J. Zhou, L. Liu, S. Huang and J. Cai, *Microporous Mesoporous Mater.*, 2021, **310**, 110662.
- 69 X. Yuan, S. P. Zhuo, W. Xing, H. Y. Cui, X. D. Dai, X. M. Liu and Z. F. Yan, *J. Colloid Interface Sci.*, 2007, 310, 83–89.
- 70 L. Tang, Y. Cai, G. Yang, Y. Liu, G. Zeng, Y. Zhou, S. Li, J. Wang, S. Zhang, Y. Fang and Y. He, *Appl. Surf. Sci.*, 2014, 314, 746-753.
- 71 G. P. Hao, W. C. Li, S. Wang, S. Zhang and A. H. Lu, *Carbon*, 2010, **48**, 3330–3339.
- 72 S. Liu, Y. Wang, B. Wang, J. Huang, S. Deng and G. Yu, *J. Cleaner Prod.*, 2017, **168**, 584–594.
- 73 P. K. Tripathi, M. Liu, L. Gan, J. Qian, Z. Xu, D. Zhu and N. N. Rao, *J. Mater. Sci.*, 2013, **48**, 8003–8013.
- 74 X. Zhuang, Y. Wan, C. Feng, Y. Shen and D. Zhao, *Chem. Mater.*, 2009, **21**, 706–716.